Supplementary Information: Composition-Induced Type I and Direct Bandgap Transition Metal Dichalcogenides Alloy Vertical Heterojunctions

Songsong Zhou,[†] Jinliang Ning,[‡] Jianwei Sun,[‡] and David J. Srolovitz[*,†,¶,§]

[†]*Department of Materials Science and Engineering, University of Pennsylvania, Philadelphia, Pennsylvania 19104, USA*

[‡]*Department of Physics and Engineering Physics, Tulane University, New Orleans, Louisiana, 70118, USA*

[¶]*Department of Mechanical Engineering and Applied Mechanics, University of Pennsylvania, Philadelphia, Pennsylvania 19104, USA*

[§]*Department of Materials Science and Engineering, City University of Hong Kong, Hong Kong SAR*

E-mail: srol@seas.upenn.edu

Cluster expansion and special quasirandom structures

The structures of ordered and disordered alloy are determined by cluster expansion (CE)[1] and special quasirandom structures (SQS) approach,[2,3] respectively. The CE approach is based upon a generalized Ising model, where any configuration of N-sites in a binary substitutional alloy may be represented by a vector $\sigma_i = (\sigma_1, \sigma_2, ... \sigma_N)$, where $\sigma_i = +1$ or -1 represents the occupancy of lattice site i by one or the other of the two elemental species. The internal energy of any configuration is $E(\sigma) = \sum_\alpha m_\alpha J_\alpha \langle \Pi_\alpha \sigma_i \rangle$, where α is a cluster, representing a specific class of interaction (e.g., first nearest pair interactions); m_α is a multiplicity that accounts for the fact that there are redundant representations of the same cluster; J_α is the interaction energy coefficient associating with cluster α; and the brackets (i.e., correlation function) denote the spin product over all available sites of a given cluster. The energy coefficients may be obtained by fitting several configurations and their energies obtained through DFT calculations; since $E(\sigma)$ converges quickly with respect to the number of clusters, only a few clusters are required. Then, given $E(\sigma)$, one easily finds the ground state configuration. For a random alloy, the theoretical value of the correlation function of a k-atom cluster is $(2x - 1)^k$, where x is the composition. The SQS approach is designed to find the arrangement of atoms in a finite size supercell that provides the best fit to these correlation functions. This can be used to simulate the properties of a random alloy.

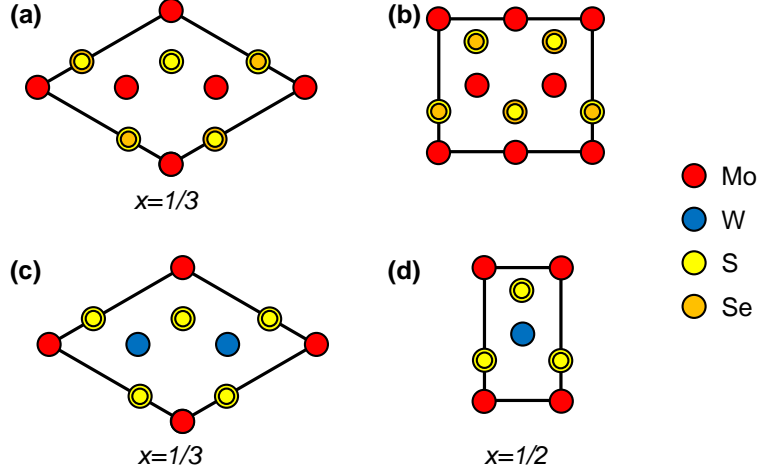# Ordered structures obtained from cluster expansion

Figure 1: The ordered ground state structures obtained by cluster expansion method for the (a) mixed anion alloy at $x = 1/3$, (b) mixed anion alloy at $x = 1/2$, (c) mixed cation alloy at x=1/3 and (d) mixed cation alloy at $x = 1/2$. The structures at $x = 2/3$ can be obtained by exchanging the two mixed species at $x = 1/3$. The red, blue, yellow and orange circles denote Mo, W, S and Se atoms, respectively. The larger and smaller circles denote the atoms in the top and bottom atomic plane, respectively.

CBM and VBM difference of TMD alloy heterojunction

The valence band maximum and conduction band minimum difference as a function of composition x in six pseudo-binary alloy heterojunctions. The energy band differences are defined as $\Delta E^{\mathrm{CBM}} = E^{\mathrm{CBM}}(x) - E^{\mathrm{CBM}}(y)$ and $\Delta E^{\mathrm{VBM}} = E^{\mathrm{VBM}}(x) - E^{\mathrm{VBM}}(y)$.
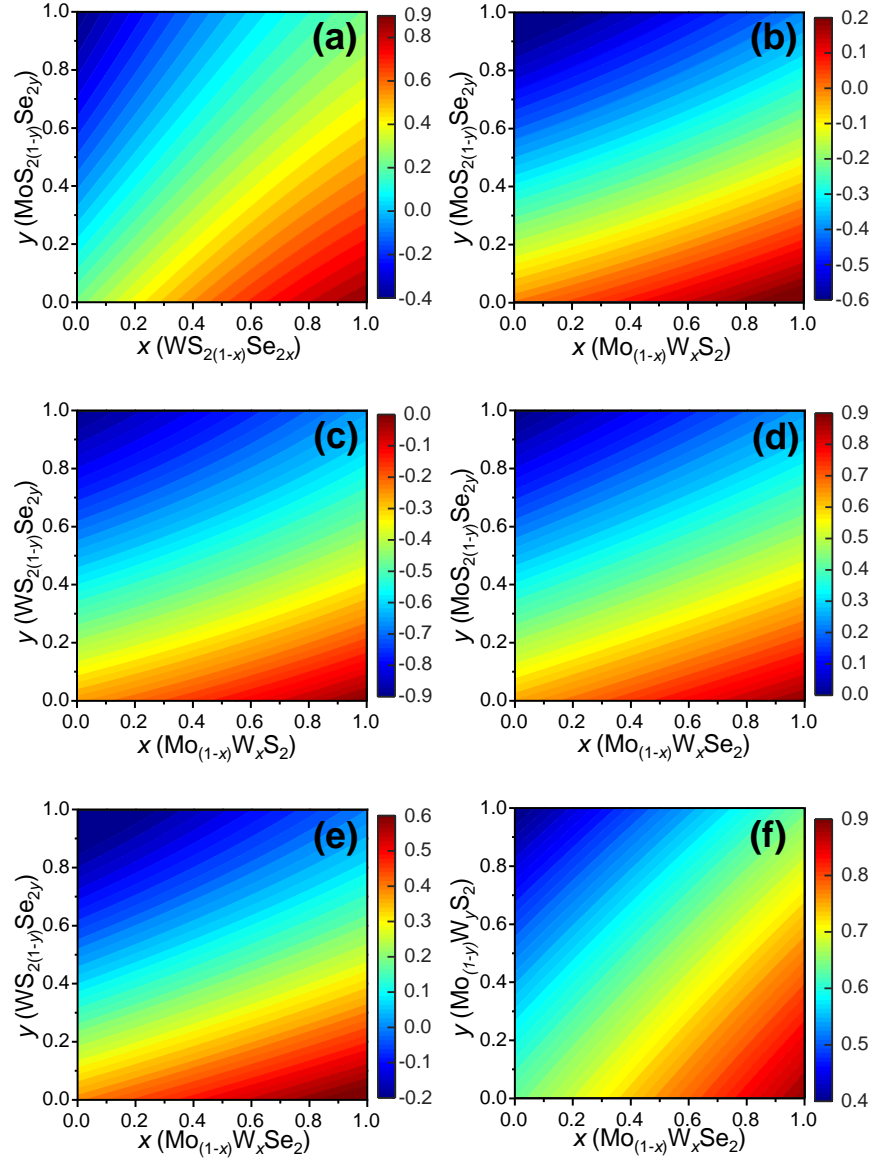
Figure 2: The valence band maximum difference for six pseudo-binary alloy heterojunctions.
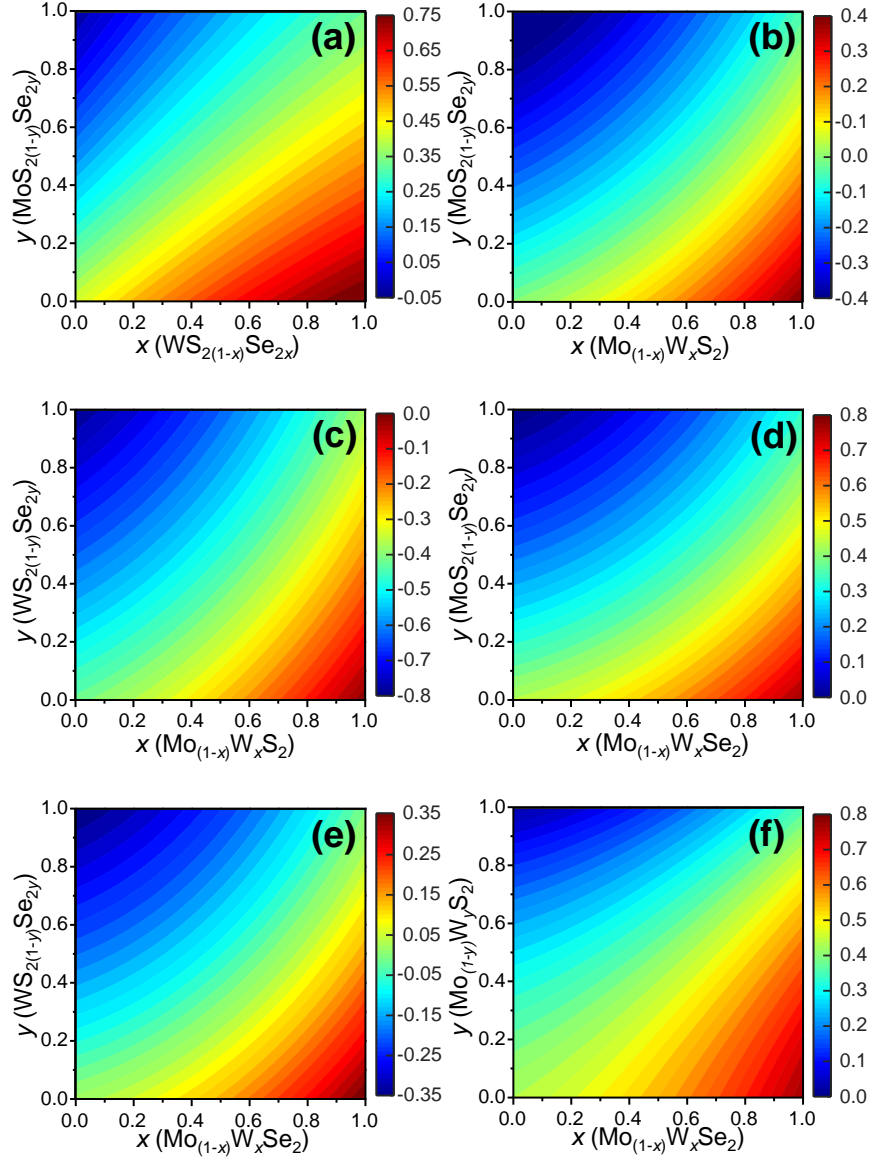
Figure 3: The conduction band minimum difference for six pseudo-binary alloy heterojunctions.

Comparison between SCAN and other methods

Table 1 summarizes the comparison between the predictions of the VBM, CBM and band gap for four different pure TMDs based on the meta-GGA functional SCAN, the GW approximation and HSE06 hybrid functional. The data from Ref. 4 and Ref. 5 was extracted from figures. SCAN generally gives band gaps slightly smaller than those obtained with GW and HSE06. In comparison with HSE06 results from Ref. 6 and Ref. 7, SCAN yields very close band gaps for WS_2 and WSe_2, but smaller band gaps for MoS_2 and $MoSe_2$ cases. The VBM predicted by SCAN is in good agreement with both the GW and HSE06 predictions, while the CBM is generally smaller than predicted with GW and HSE06. For band alignment, our SCAN results predict that all TMD heterojunctions are Type II, in agreement with Ref. 5 (GW) /Ref. 7 (HSE06) and experiment (Ref. 8). But in Ref. 6, the $MoSe_2/WS_2$ heterojunction was predicted to be of Type I. The conduction band minimum of $MoSe_2$ and WS_2 in Ref. 4 are very close to each other.

Table 1: Comparison between the VBM, CBM and band gap predictions made using SCAN, GW and HSE06.

	SCAN			GW			HSE06		
	VBM	CBM	gap	VBM	CBM	gap	VBM	CBM	gap
MoS_2	-6.18	-4.39	1.79	-6.24[c]	-3.89[c]	2.35[c]	-6.33[a] -6.27[d] -6.22[b]	-4.18[a] -4.25[d] -4.03[b]	2.15[a] 2.02[d] 2.19[b]
WS_2	-5.93	-3.97	1.96	-5.87[c]	-3.59[c]	2.28[c]	-5.86[a] -5.82[d] -6.00[b]	-3.77[a] -3.84[d] -3.64[b]	2.09[a] 1.98[d] 2.36[b]
$MoSe_2$	-5.54	-3.95	1.59	-5.55[c]	-3.58[c]	1.97[c]	-5.54[a] -5.59[d] -5.59[b]	-3.67[a] -3.87[d] -3.64[b]	1.87[a] 1.72[d] 1.95[b]
WSe_2	-5.29	-3.60	1.69	-5.18[c]	-3.22[c]	1.96[c]	-5.12[a] -5.16[d] -5.36[b]	-3.37[a] -3.53[d] -3.29[b]	1.75[a] 1.63[d] 2.07[b]

[a] Ref. 7
[b] Ref. 4
[c] Ref. 5
[d] Ref. 6

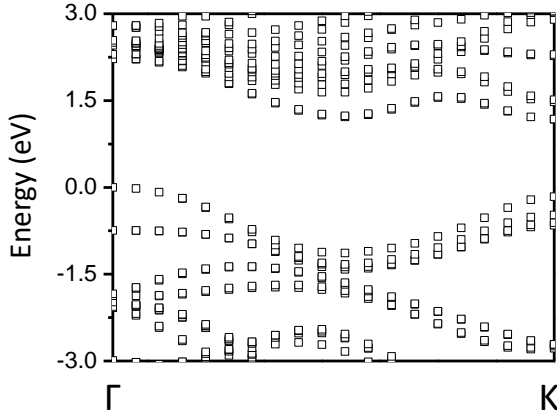# Band structure of MoS_2/WS_2

Figure 4: The band structure of unrotated MoS_2/WS_2 heterojunction. The zero of energy is set to the valence band maximum for reference.

Interlayer distance and Van der Waals correction

Different Van der Waals (vdw) corrections methods are tested and compared. We first calculated the VBM at Γ, VBM at K and CBM at K in unrotated MoS_2/WS_2 heterojunction as a function of interlayer distance, as shown in Fig. S5. Unsuperisingly the VBM at K and CBM at K are independent of interlayer distance, while VBM at Γ is sensitive to that. We then calculated the interlayer distance using different vdw corrections including DFT-D3, Tkatchenko-Scheffler (TS, employed in main text), optB86b-vdW and optB88-vdW, the calculation results are marked by dash lines. The experimental interlayer distance of bulk MoS_2 and WS_2 are of 6.15 and 6.16 Å, respectively.[9,10] And thus we may approximate the interlayer distance of the heterojunction as 6.155 Å. The interlayer distance calculated by PBE without vdw correction is 6.88 Å, which is much larger than experimental value. However, all vdw corrections yield interlayer distance close to experimental value (no more than 0.1 Ådifference). Such small difference in interlayer distance will not lead to any significant variation of VBM at Γ, as shown in Fig. S5.
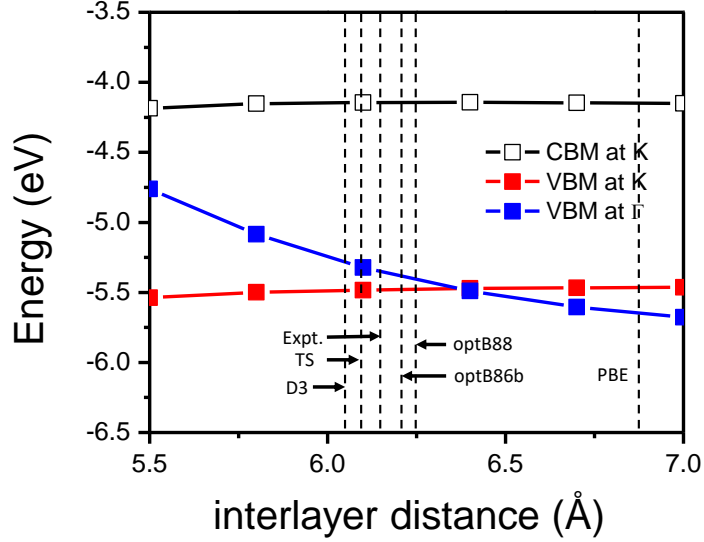
7

Figure 5: The energy level at Γ and K as a function of interlayer distance. The dash lines represent the interlayer distance calculated using different vdw corrections, as indicated.

Atomic structure of twisted heterojunction

The top view of twisted heterojunctions used in Fig.7 of main text are shown in Fig. S6.

Detail of geometric model

To measure the overlap area, we build a model of two monolayers. A small rhombus monolayer is placed on top of a large bottom monolayer. The top and bottom monolayer have lattice constant a_+ and a_-, respectively. a_+ can be assumed as 1 and parameter $p_1 = a_-/a_+$ defines the lattice mismatch. The $p_2 = R_+/a_+$ and $p_3 = R_-/R_+$ define the circle radius in two monolayers. The edge length of top monolayer is na_+ ($n \in \mathbb{Z}^+$). Obviously, the overlaping area $S_{overlap}$ is a function of p_1, p_2, p_3, n and θ. With given parameter p_1, p_2, p_3, n, an index can be defined to describe the interlayer interaction as a function of rotation angle θ:

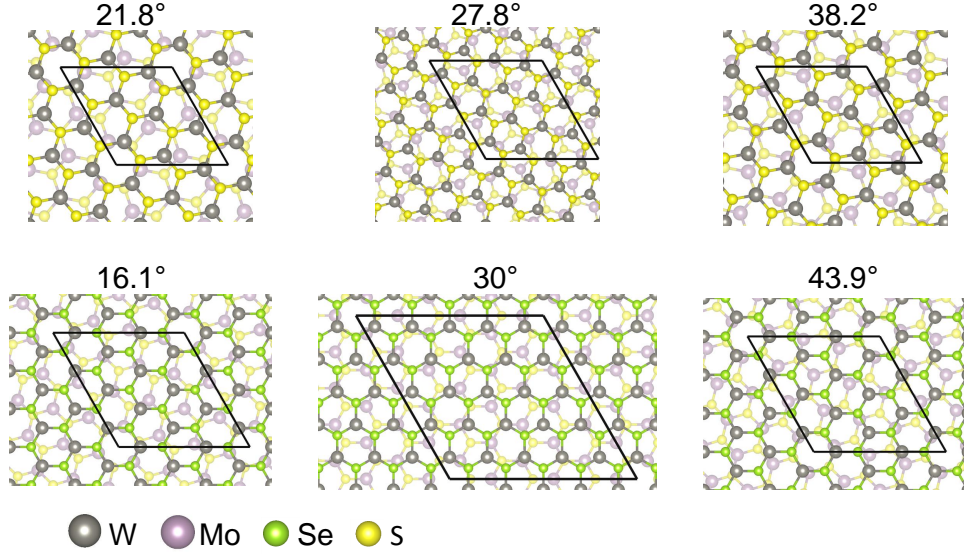$$I(\theta) = 1 - \left.\frac{S_{overlap}(\theta)}{S_{total}}\right|_{p_1,p_2,p_3,n} \tag{1}$$

Figure 6: The atomic structures (top view) of twisted heterojunctions. The grey, purple, green and yellow spheres denote W, Mo, Se and S atoms, respectively. The spheres with lighter shading denote atoms in the lower layer.

where $S_{overlap}(\theta)$ is the overlaping area between circles in two monolayers, and S_{total} is the total area of circles in top monolayer.

Effect of lattice mismatch parameter p_1

The parameter p_1 defines the lattice mismatch between two monolayers. Withour lose of generality, we assume $a_+ \leq a_-$, so that $p_1 \geq 1$. In Fig. S7, we show how the index $I(\theta)$ change when increase p_1 from 1 (lattice-matched case such as MoS_2/WS_2) to 1.044 (lattice-mismatchd case, such as MoS_2/WSe_2). Here the other parameters chosen are: $p_2 = 1/2\sqrt{3}$, p_3=1, n=22. It is clearly that with p_1 increasing, the peaks near 0 and 60° become shorter and wider, while in the middle angular range the index is still a constant indepent of p_1 and θ.
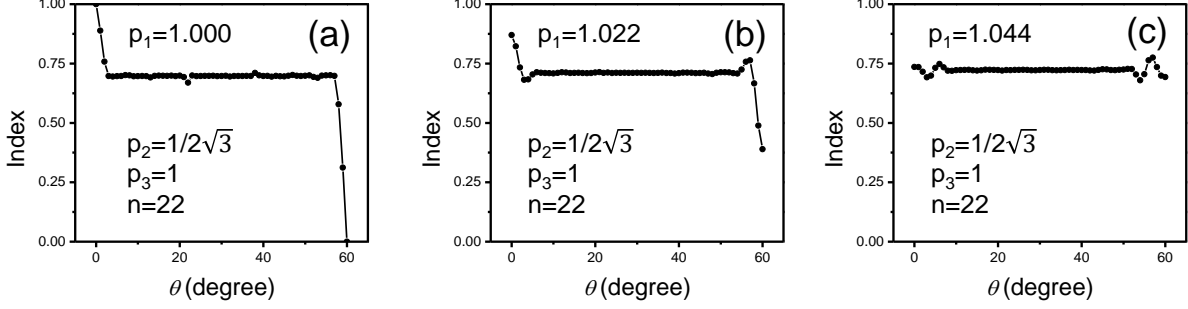
Figure 7: (a)-(c), the index $I(\theta)$ when p_1=1, 1.022 and 1.044, respectively.

Effect of circle radius parameter p_2 and p_3

The parameter p_2 and p_3 define the circle radius R_+ and R_- in top and bottom monolayers. In Fig. S8 (a)(b), we show that index $I(\theta)$ as a function of p_2 for p_1=1 and 1.044, respectively. In Fig.S 8 (c)(d), we show that index $I(\theta)$ as a function of p_3 for p_1=1 and 1.044, respectively. Clearly, decreasing p_2 and p_3 do not change the general trend but only increase the constant level in middle angular range. The parameter used in Fig. S8 are: (a)-(b), n=22 and p_3=1; in (c)-(d), n=22 and $p_2 = 1/2\sqrt{3}$.

Effect of top monolayer size n

The index $I(\theta)$ as a function of n is shown in Fig. S9. Here we set other parameters $p_2 = 1/2\sqrt{3}$ and p_3=1. When $p_1 = 1$, it is clearly that changing n does not change the general trend. The only difference is that as n incearsing, the width of peaks near 0 and 60° become smaller, so the peaks become more sharp. Similarly, when $p_1 = 1.044$, changing n does not change the general trend. In the middle angular range, the index is always a constant. But changing n will change the fluctuation regions (near 0 and 60°) in their width and height.

Comparison of flake approach and supercell approach

We used the flake approach to calculate the $S_{overlap}$ and index $I(\theta)$, where a limited size of monolayer flake are placed and rotated on the top of a large bottom monolayer. This
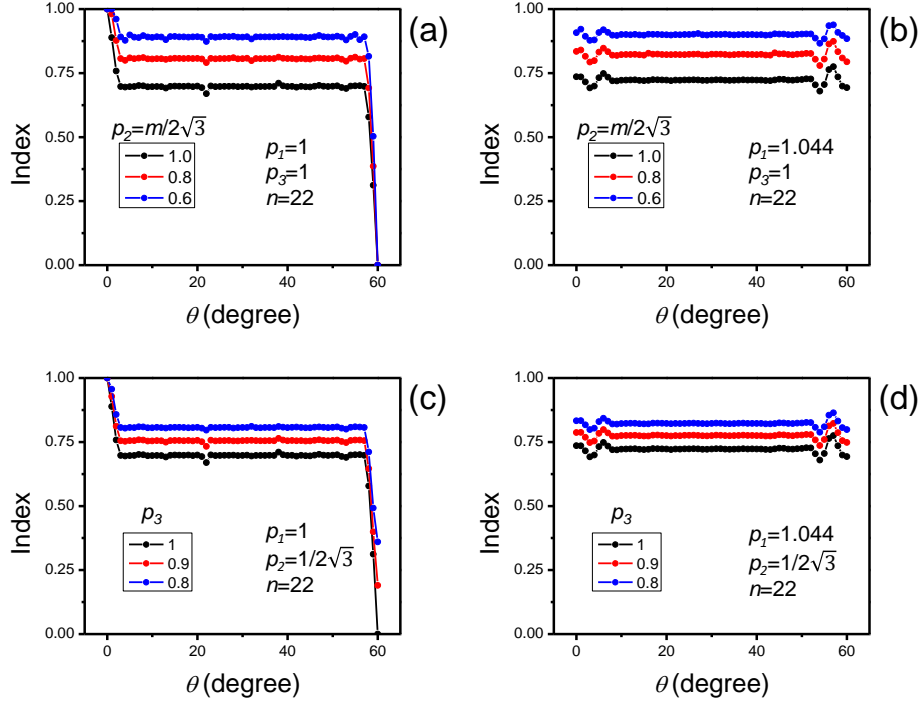
Figure 8: (a)-(b), the index $I(\theta)$ when $p_2=m/2\sqrt{3}$, where $m = 1.0, 0.8, 0.6$ at the case of $p_1=1$ (a), and $p_1=1.044$ (b), respectively; (c)-(d), the index $I(\theta)$ when $p_3=1$, 0.9, 0.8 at the case of $p_1=1$ (c), and $p_1=1.044$ (d), respectively.
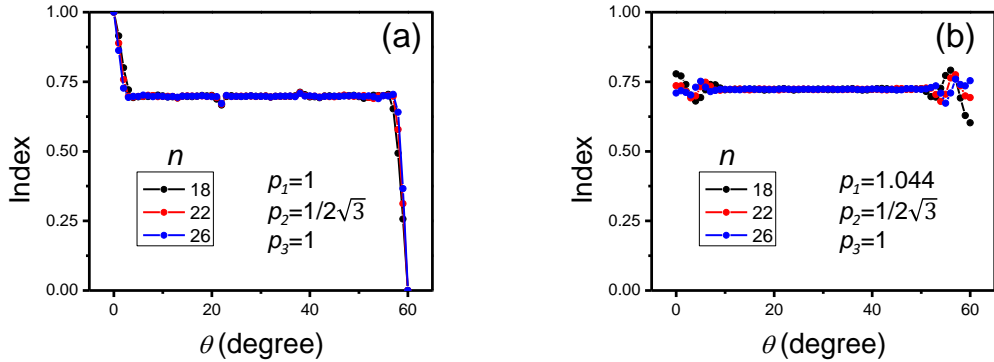

Figure 9: (a)-(b): the index $I(\theta)$ when $n=18$ (black), 22 (red) and 26 (blue), at $p_1 = 1$ (a) and $p_1 = 1.044$ (b), respectively.

11

approach allows us to obtain continuous numeric result of $I(\theta)$ but do not describe the true infinite large heterobilayer in supercell cases. So here to further validify our flake approach, we calculated a set of $I(\theta)$, following the same definition in main text by using supercell instead of flake, i.e. $n \to \infty$. The parameter used here is $p_2 = 1/2\sqrt{3}$ and $p_3=1$, for flake approach, $n=22$. The result is shown in Fig.S 10. Clearly, the index obtained by two approach match perfectly with each other.
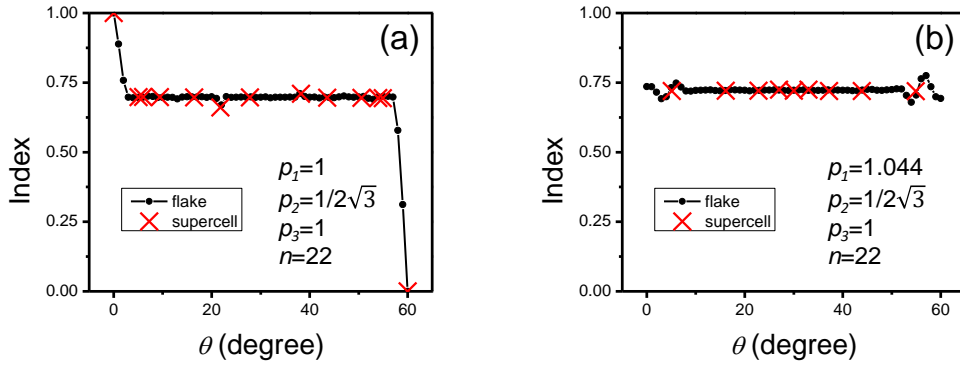

Figure 10: (a)-(b): the index $I(\theta)$ obtained by flake approach (black dots) and supercell approach (red cross), at $p_1 = 1$ (a) and $p_1 = 1.044$ (b), respectively.

References

(1) Sanchez, J. M.; Ducastelle, F.; Gratias, D. *Physica A: Statistical Mechanics and its Applications* **1984**, *128*, 334–350.

(2) Zunger, A.; Wei, S.-H.; Ferreira, L. G.; Bernard, J. E. *Physical Review Letters* **1990**, *65*, 353.

(3) Wei, S.-H.; Ferreira, L. G.; Bernard, J. E.; Zunger, A. *Physical Review B* **1990**, *42*, 9622.

(4) Pandey, M.; Jacobsen, K. W.; Thygesen, K. S. *The Journal of Physical Chemistry C* **2016**, *120*, 23024–23029.

(5) Gong, C.; Zhang, H.; Wang, W.; Colombo, L.; Wallace, R. M.; Cho, K. *Applied Physics Letters* **2013**, *103*, 053513.

(6) Kang, J.; Tongay, S.; Zhou, J.; Li, J.; Wu, J. *Applied Physics Letters* **2013**, *102*, 012111.

(7) Özçelik, V. O.; Azadani, J. G.; Yang, C.; Koester, S. J.; Low, T. *Physical Review B* **2016**, *94*, 035125.

(8) Keyshar, K.; Berg, M.; Zhang, X.; Vajtai, R.; Gupta, G.; Chan, C. K.; Beechem, T. E.; Ajayan, P. M.; Mohite, A. D.; Ohta, T. *ACS nano* **2017**, *11*, 8223–8230.

(9) Schutte, W.; De Boer, J.; Jellinek, F. *Journal of Solid State Chemistry* **1987**, *70*, 207–209.

(10) Srivastava, S. K.; Avasthi, B. N.; Mathur, B. K. *Journal of materials science letters* **1984**, *3*, 671–673.